RSC Advances

PAPER

View Article Online
View Journal | View Issue



Cite this: *RSC Adv.*, 2023, **13**, 6346

# High strontium adsorption performance of layered zirconium phosphate intercalated with a crown ether

Lina Wu, [abc] Huiping Wang,*[bc] Xiangqian Kong,[bc] Haibo Wei, [bc] Sheng Chen[bc] and Lisheng Chi *[bc]

Effective removal of strontium isotopes in radioactive waste streams has important implications for the environment and the sustainable development of nuclear energy. In this work, a zirconium phosphate/18-crown-ether-6 (ZrP/18C6) composite was prepared using the intercalation method by loading crown ether into zirconium phosphate. The composite was structurally and morphologically characterized by XRD, FT-IR, XPS, and SEM. The adsorption experiments of $Sr^{2+}$ onto the ZrP/18C6 composite were conducted as a function of temperature, pH, $Sr^{2+}$ concentration and competing ions. The results indicate ZrP/18C6 can adsorb 98.6% of $Sr^{2+}$ within 30 minutes at an $Sr^{2+}$ concentration of 100 mg $L^{-1}$ and maintain a high removal rate with a distribution coefficient of $7 \times 10^5$ mL $g^{-1}$ when $Sr^{2+}$ is at a low level of 4.28 mg $L^{-1}$. The ZrP/18C6 composite reached a maximum adsorption capacity of 195.74 mg $g^{-1}$ at an $Sr^{2+}$ concentration of 380 mg $L^{-1}$, which is significantly higher than the 43.03 mg $g^{-1}$ of α-ZrP. The adsorption performance of $Sr^{2+}$ onto ZrP/18C6 is not significantly affected by temperature, pH and competing ions. Furthermore, the adsorption kinetics and thermodynamics were analyzed based on the adsorption data obtained in the present work. It is shown that the adsorption of $Sr^{2+}$ onto ZrP/18C6 follows the pseudo-second-order model and the Langmuir monolayer model, respectively. Additionally, the adsorption mechanism of $Sr^{2+}$ by ZrP/18C6 is discussed.

Received 5th December 2022
Accepted 15th February 2023

DOI: 10.1039/d2ra07757d

rsc.li/rsc-advances



## 1 Introduction

Sr-90 is one of the fission products decayed from U-235 when a nuclear power plant is in operation.[1] It has a long half-life of 29 years and is one of the most radioactive nuclides in nuclear waste streams.[2] Moreover, due to the high similarity between strontium and calcium in chemical properties, on entering human body, strontium can be easily adsorbed by bone, which could cause bone cancer and leukemia.[3,4] Therefore, efficient removal of strontium isotopes from nuclear wastes is of great importance.

Many studies have been conducted on removal of strontium isotopes from nuclear waste streams. The main methods studied include chemical precipitation,[5] solvent extraction,[6,7] membrane treatment,[8,9] biological methods,[10,11] and adsorption methods.[12–14] Among these methods, the adsorption method has advantages over other methods in treatment efficiency, chemical reagent dosage, and separation cost. Therefore, in the last decades, a lot of adsorbents have been developed.[15–17] However, the adsorbent materials for the removal of Sr isotopes with a fast adsorption rate, good stability, and excellent adsorption performance have been rarely reported.[18,19]

α-ZrP ($Zr(HPO_4)_2 \cdot H_2O$) is a two-dimensional layered phosphate with a layer spacing of 0.76 nm and a large number of P–OH groups between the layers.[20,21] The hydrogen protons in P–OH groups can be exchanged with other metal ions,[22–24] demonstrating their good ion-exchange properties. Furthermore, the zirconium phosphate material has a good adsorption capacity for alkali metals and alkaline earth metals, as well as for Sr-90 in radioactive waste streams.[12,25,26] In addition, as an inorganic adsorbent, it has good thermal stability, acid resistance, good mechanical strength, and ease of synthesis.[22,25] As the weak interlayer force makes the α-ZrP layer spacing adjustable, the guest molecules can be inserted under certain conditions to change the properties of the host or the guest.[23,27,28] The pre-intercalation method is generally used to prepare composite of host and guest materials, and the pre-intercalation materials used to adjust interlayer space of the zirconium phosphate are mainly amine molecules.[28] After insertion of an amine molecule, the carbon skeleton of the amine molecule and the layer of the zirconium phosphate are maintained as a single parallel structure or a double-layer oblique insertion structure, which plays a vital role in

[a]College of Chemistry, Fuzhou University, Fuzhou, Fujian 350108, China
[b]Fujian Science and Technology Innovation Laboratory for Optoelectronic Information of China, Fuzhou 350116, China
[c]Fujian Key Laboratory of Fuel and Materials in Clean Nuclear Energy System, Fujian Institute of Research on the Structure of Matter, CAS, Fuzhou, Fujian 350002, China. E-mail: lchi@fjirsm.ac.cn

expanding the interlayer space.[29,30] As a result, a number of adsorbents based on zirconium phosphate material with excellent adsorption properties have been developed.[27,31]

The crown ether is composed of multiple ethoxy (C–C–O) units, and the multiple powered oxygen atoms in the structure allow it to form host–guest complexes with alkali and alkaline earth metal ions.[32,33] As the diameter of $Sr^{2+}$ (0.23 nm) is close to the size of the cavity in 18-crown-ether-6 (18C6) and its derivatives, which is in the range of 0.26–0.32 nm, $Sr^{2+}$ can enter the cavity to interact with O atoms in 18C6 to form stable complexes.[19,34] As a result, the 18C6 has become the most studied extractant in the removal of Sr-90 from highly radioactive waste streams.[7,35–38] However, as an organic material, post-treatment of the crown ether after nuclear waste adsorption poses a challenge.[38]

In this experiment, the target products were synthesized by a pre-intercalation method. The pre-supporter material used in zirconium phosphate is *n*-butylamine molecule.[22] The interlayer space in zirconium phosphate is about 1.8 nm after intercalating with the *n*-butylamine molecule, which is close to the molecular width of 18-crown-ether-6.[28,39] Therefore, *n*-butylamine was finally selected as the intercalator to prepare the pre-propellant material in this study. In the present work, based on the structure character of α-ZrP, 18-crown-ether-6 was successfully inserted into the interlayers to form the ZrP/18C6 composite, which is evaluated for its adsorption properties and stability in the removal of strontium ions from simulated nuclear wastes. The study reveals that ZrP/18C6 is a promising adsorbent material for the removal of strontium ions from nuclear waste streams.

# 2 Experimental

## 2.1 Chemicals

Zirconium oxychloride octahydrate ($ZrOCl_2 \cdot 8H_2O$, 99%), orthophosphoric acid ($H_3PO_4$, 85 wt%), hydrofluoric acid (HF, 99%), *n*-butylamine ($CH_3(CH_2)_3NH_2$, 99%), anhydrous ethanol ($CH_3CH_2OH$, 99.7%), strontium nitrate (Sr $(NO_3)_2$, 99%), sodium nitrate ($NaNO_3$, 99%), and potassium nitrate ($KNO_3$, 99%) were purchased from Shanghai Sinopharm Chemical Reagent Company. 18-crown-ether-6 ($C_{12}H_{24}O_6$, 98%) was obtained from Shanghai Aladdin Biochemical Technology Company. All chemicals above were used as received without further purification. Ultra-pure water was provided by ultra-pure water purification equipment (Direct-Q5UV Millipore, 18.2 MΩ cm @ 25 °C).

## 2.2 Characterization

X-ray diffraction (XRD) was performed on a Rigaku Miniflex 600 in the $2\theta$ range from 3° to 80° with a scan rate of 5° $min^{-1}$ to characterize the crystal structure of the samples before and after adsorption of $Sr^{2+}$ ions. Fourier transform infrared spectroscopy (FT-IR) was used to characterize the functional groups of the composites. The IR spectra were collected on a Bruker Optics Vertex70 infrared spectrometer in a scan range from 400 $cm^{-1}$ to 4000 $cm^{-1}$. The elemental composition and elemental electron binding energies of the composites were characterized by X-ray photoelectron spectroscopy (XPS) and obtained on a ThermoFisher Escalab 250Xi X-ray photoelectron spectrometer. The morphology and microstructure of the adsorbents were observed by Hitachi SU8010 field emission scanning electron microscope (SEM). Thermogravimetric analysis (TGA) was conducted using a Netzsch STA 499F3 type thermal analyzer to determine the thermal stability of the samples in the temperature range from 30 °C to 950 °C under a nitrogen gas flow. The ion concentration in the solution was measured using a PerkinElmer Avio 200 inductively coupled plasma emission spectrometry (ICP-OES).

## 2.3 Preparation of ZrP/18C6 composites

The α-ZrP was synthesized using the fluorine reflux method as follows.[21,35] 100 mL of 3 mol $L^{-1}$ phosphoric acid ($H_3PO_4$) was mixed well with 9.72 g of zirconium oxychloride octahydrate ($ZrOCl_2 \cdot 8H_2O$), followed by adding 6 mL of hydrofluoric acid (HF) and refluxing at a temperature of 100 °C for 24 hours. After cooling, the reaction product was washed with ultrapure water several times and dried in a vacuum oven at 70 °C overnight. The product was identified by XRD to be α-zirconium phosphate (α-ZrP).

Then, 1 g of α-zirconium phosphate (α-ZrP) was dispersed into 100 mL of 1 mol $L^{-1}$ *n*-butylamine solution, followed by stirring in an oscillator for 5 days. The reaction product was separated by centrifugation and washed several times to remove the excess *n*-butylamine. The product was dried at 70 °C and named β-zirconium phosphate (β-ZrP).

Finally, β-ZrP and 18-crown-ether-6 were uniformly dispersed into anhydrous ethanol solution. The mixed solution was shaken in an oscillator for 5 days. The final product was separated by centrifugation, washed several times with ultrapure water, and dried in a drying oven at 70 °C. The obtained zirconium phosphate/crown-ether composite (namely, ZrP/18C6) was white powder and used for the following studies.

## 2.4 Batch adsorption experiments

Batch adsorption experiments of $Sr^{2+}$ on the α-ZrP and ZrP/18C6 materials were performed in polyethylene centrifuge tubes. 20 mg adsorbent was added to 20 mL of the $Sr^{2+}$ solution and the solution was shaken in an oscillator for 6 h until adsorption equilibrium was reached. The adsorbent was removed with an injection filter and the concentration of $Sr^{2+}$ ions in the solution was measured using ICP-OES before and after adsorption. Due to large variation in nuclear waste streams, the adsorption performance is investigated in the aqueous solution, which is partly related to the actual nuclear waste environments.

In this study, the effects of pH, temperature, competing ions, and initial concentration of $Sr^{2+}$ on the adsorption performance of ZrP/18C6 and α-ZrP were carried out. The solution pH was adjusted to 2, 3, 4, 5, 6, 7, 8, 9 and 10 using 0.1 mol $L^{-1}$ nitric acid and 0.1 mol $L^{-1}$ sodium hydroxide. $Na^+$ and $K^+$ were selected as competing ions for testing adsorption of $Sr^{2+}$ on ZrP/18C6. In addition, the desorption of $Sr^{2+}$ adsorbed on ZrP/18C6 was studied.

The equilibrium adsorption capacity ($Q_e$, mg $g^{-1}$), adsorption efficiency ($R$, %), and distribution coefficient ($K$, mL $g^{-1}$) of the adsorbents on strontium ions were determined using the following eqn (1)–(3):

$$Q_e = \frac{(C_o - C_e)V}{m} \quad (1)$$

$$R = \frac{C_o - C_e}{C_o} \times 100\% \quad (2)$$

$$K = \frac{(C_o - C_e)V}{C_e m} \times 1000 \quad (3)$$

where $C_o$ (mg $L^{-1}$) and $C_e$ (mg $L^{-1}$) are the concentration of $Sr^{2+}$ in the solution at the initial and adsorption equilibrium, respectively; $V$ (mL) is the volume of $Sr^{2+}$ solution; $m$ (mg) is the mass of the adsorbent used.

# 3 Results and discussion

## 3.1 Structural characterizations

**3.1.1 XRD analysis.** The XRD patterns of α-ZrP, β-ZrP, and ZrP/18C6 materials are obtained (Fig. 1). A sharp diffraction peak at 11.64° was observed in the synthesized α-ZrP sample, which corresponds to the diffraction plane (002) of JCPDS no. 34-0127, and the other diffraction peaks also match well those of the card. This confirms successful synthesis of the pure phase α-$Zr(HPO_4)_2 \cdot H_2O$ (α-ZrP).

The peak at 11.64° can be used to characterize the interlayer separation. Based on the Bragg equation expressed with the following eqn (4):

$$2d \sin\theta = n\lambda \quad (4)$$

where $d$ (nm) is the crystal plane spacing; $\theta$ is the diffraction half-angle; $\lambda$ is the wavelength; $n$ is the diffraction level.

The peak at 11.64° in α-ZrP corresponds to the interlayer separation of 0.760 nm. Intercalation of *n*-butylamine into α-ZrP forms β-ZrP, leading to expanding of the interlayer separation.[31] Therefore, the diffraction peak shifts to the lower angle at 4.91° in β-ZrP, which corresponds to the interlayer separation of 1.798 nm. This implies that *n*-butylamine was successfully inserted into zirconium phosphate. The XRD pattern of the ZrP/18C6 composite is similar to that of β-ZrP. However, the peak further shifts to a lower angle at 4.72°, which is ascribed to substitution of 18-crown-ether-6 for *n*-butylamine. Intercalation of 18-crown-ether-6 forces the interlayer space to open wider to 1.871 nm as the size of 18-crown-ether-6 is larger than *n*-butylamine. As a result, the ZrP/18C6 composite provides more room between the layers for adsorbate. As the 18-crown-ether-6 has been known as a highly selective adsorbent for $Sr^{2+}$,[34,40] the ZrP/18C6 composite could be prospective for an $Sr^{2+}$ adsorbent with high adsorption capacity.

**3.1.2 FT-IR analysis.** Functional groups of the material were characterized using infrared spectroscopy (Fig. 2). In the IR spectrum of α-ZrP, the 534 $cm^{-1}$ and 594 $cm^{-1}$ peaks are assigned to Zr–O vibrations; the 968 $cm^{-1}$ and 1251 $cm^{-1}$ peaks are due to out-of-plane and in-plane vibrations of P–OH, respectively. The 1053 $cm^{-1}$ peak is due to stretching vibration of the P–O group of $PO_4$; the 1620 $cm^{-1}$ peak is due to bending vibration of the –OH group in $H_2O$; the 3145 $cm^{-1}$ is a wide absorption peak resulting from stretching vibration of the intermolecular hydrogen bonded –OH group, and the 3512 $cm^{-1}$ and 3593 $cm^{-1}$ peaks are due to stretching vibrations of the free hydroxyl O–H group.[41]

Several new peaks appeared after *n*-butylamine was inserted into α-ZrP to replace $H_2O$. The 3556 $cm^{-1}$ peak is due to the N–H stretching vibration. The 2962 $cm^{-1}$ and 2873 $cm^{-1}$ peaks are due to stretching vibrations of the $-CH_3$ group in the inserted *n*-butylamine.[35]

When 18-crown-ether-6 was inserted into β-ZrP, the water molecule was also entered. The 3128 $cm^{-1}$ broad peak is due to stretching vibration of the –OH group, the 1037 $cm^{-1}$ peak is due to stretching vibration of the C–O–C group, and the 2960 $cm^{-1}$ peak is due to stretching vibration of the $-CH_2$ group in crown ether. The results indicate that 18-crown-ether-6 has been successfully compounded with zirconium phosphate.

**3.1.3 XPS analysis.** XPS was used to investigate the elemental characteristics and binding energies of ZrP/18C6

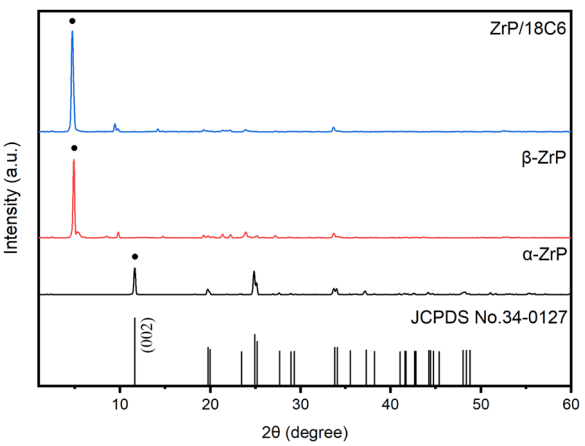


Fig. 1 XRD patterns of α-ZrP, β-ZrP, and ZrP/18C6.

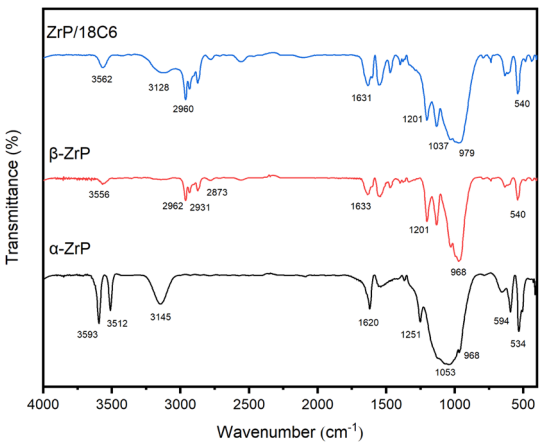


Fig. 2 FT-IR spectra of α-ZrP, β-ZrP, and ZrP/18C6.

material (Fig. 3). The comprehensive elemental information was obtained by Gauss–Lorentz fitting of C 1s and O 1s. The full scan spectrum in Fig. 3(a) shows that the material consists of Zr, P, C, and O elements. Fig. 3(b) shows that the C 1s peak can be deconvoluted to three peaks at 284.80 eV, 286.30 eV, and 288.73 eV, respectively, indicating carbon exists in three different states of C–C/C–H, C–OH, and C–O–C, respectively.[14] Fig. 3(c) presents deconvolution of the O 1s peak to three types of peaks at 531.11 eV, 532.55 eV and 533.43 eV.[42,43] Therefore, oxygen in the ZrP/18C6 exists in three different states of –OH, P–O and C–O–C, respectively.[42] This is consistent with the results observed in IR. The XPS analysis further confirms that 18-crown-ether-6 has been inserted into zirconium phosphate.

**3.1.4 SEM analysis.** The morphologies of α-ZrP and ZrP/18C6 were characterized by scanning electron microscopy (Fig. 4). It can be observed that the ZrP/18C6 is comprised of a large number of hexagonal units with a flat and smooth surface, which is consistent with the α-ZrP morphology. The side view in Fig. 4(b) clearly shows that the ZrP/18C6 material is a lamellar structure.

### 3.2 Stability

In practice, an adsorbent must demonstrate fair stability for its application.[31] The thermal stability of the composites was tested by thermogravimetry under the nitrogen atmosphere (Fig. 5(a)). In the temperature from 30 °C to 950 °C, the weight loss is mainly composed of three parts. The first weight loss occurs at the temperature ≦120 °C due to the evaporation of water from the surface of the material. The second weight loss occurs at the temperature between 120 °C and 300 °C due to loss of crystallized water within the structure, which is the main weight loss. The final weight loss is mainly due to escape of inserted *n*-butylamine and 18-crown-ether-6 in the interlayer at the temperature from 300 °C to 600 °C.

The acid resistance of the adsorbents was tested for possible application in treatment of nuclear waste streams. The acid resistance was investigated by measuring leakage rates of P and Zr after soaking the 10 mg materials in 20 mL nitric acid with different concentrations for 24 hours at room temperature (Fig. 5(b)). The leakage rate of ion is calculated using eqn (5).

$$\text{Leakage rate} = \frac{C \times V}{m} \times 100\% \quad (5)$$

where $C$ (mg $L^{-1}$) is the concentration of leakage ion in the solution; $V$ (L) is the volume of nitric acid solution used; $m$ (mg) is the mass of the soaking adsorbent.

With the increase in nitric acid concentration, the leakage rates of P and Zr are up to 2% and 6%, respectively. The low leakage rates of P and Zr indicate that the composites have good stability under the acid conditions tested.

### 3.3 Adsorption performance of adsorbents

**3.3.1 Effect of crown ether dosage on $Sr^{2+}$ adsorption.** Different mass ratios of 18-crown-ether-6 to zirconium phosphate in composites were tested to optimize adsorption performance. In this test, the mass ratios of 18-crown-ether-6 to zirconium phosphate at 0.3 : 1, 0.5 : 1, 0.75 : 1, 1 : 1, 2 : 1, and 3 : 1 was used, and all the adsorption experiments were performed under the same conditions (Fig. 6(a)). The results show that the

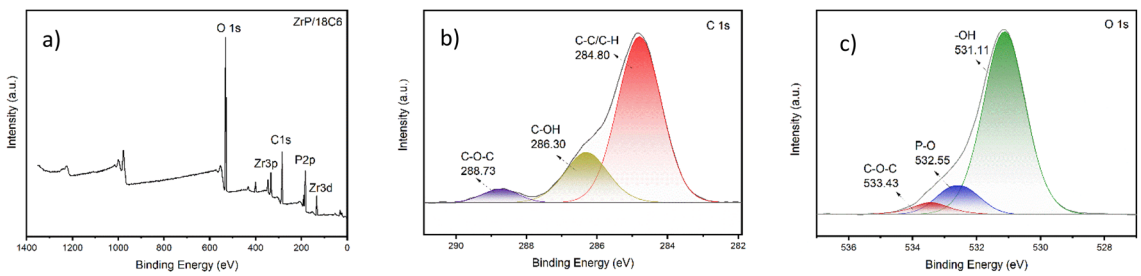


Fig. 3 XPS spectra of ZrP/18C6. (a) Full. (b) C 1s. (c) O 1s.

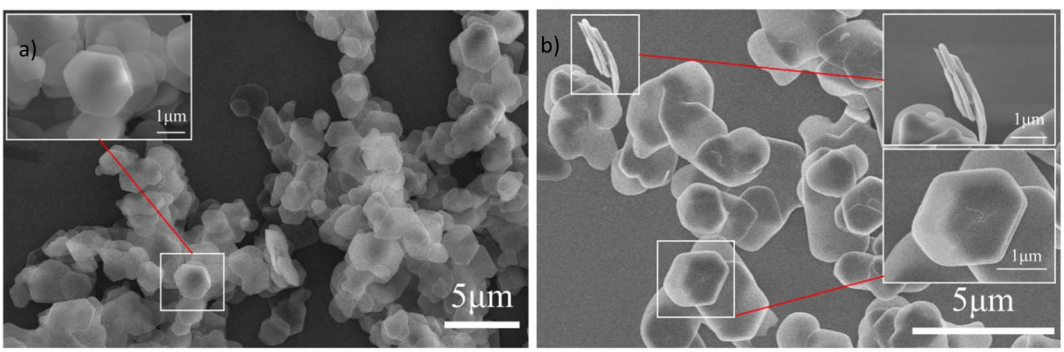


Fig. 4 SEM images of adsorbents, (a) α-ZrP, (b) ZrP/18C6.

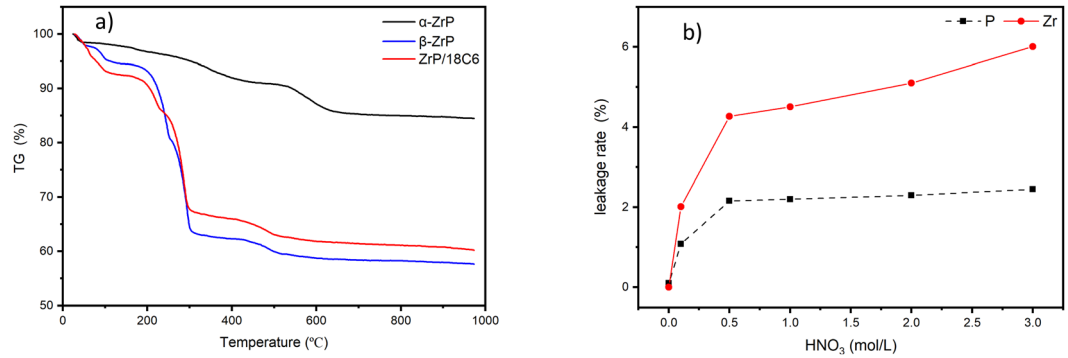


Fig. 5 Stability investigation of adsorbents. (a) TGA curves for α-ZrP, β-ZrP, and ZrP/18C6 at the temperature from 30 °C to 950 °C. (b) Leakage rates of P and Zr for ZrP/18C6 at different $HNO_3$ concentrations for 24 h.

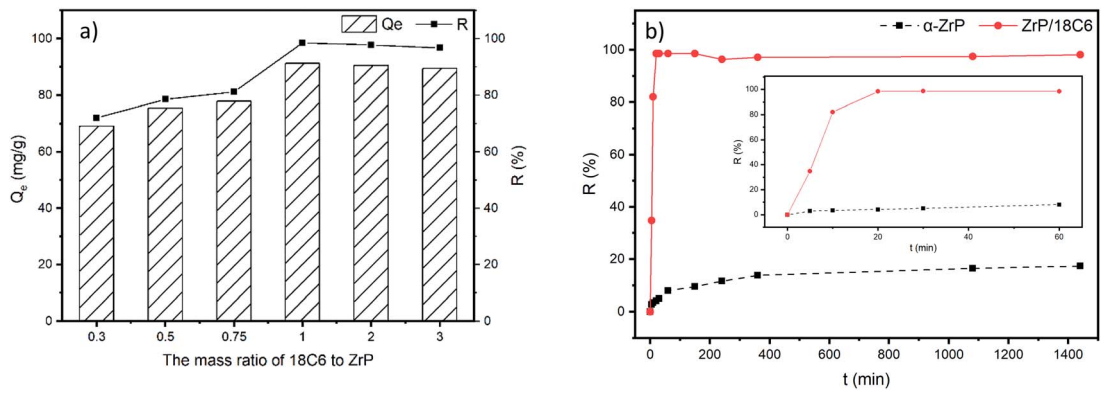


Fig. 6 (a) The effect of mass ratio of 18-crown-ether-6 to zirconium phosphate. (b) Effect of contact time.

adsorption capacity and removal rate of the composites for $Sr^{2+}$ increased significantly with increasing the inserted amount of 18-crown-ether-6. The adsorption capacity reached the maximum at a mass ratio of 1 : 1, followed by slightly decreasing when the mass of crown ether was further increased. This can be ascribed to substitution of 18C6 for *n*-butylamine located in the interlayer of zirconium phosphate, which increases the adsorption sites due to the larger size of 18C6. However, excessive insertion leads to a reduction in the free space between layers.[35] This increases the difficulty of $Sr^{2+}$ entering the interlayer, which in turn reduces the adsorption capacity. Based on the results obtained in this test, the 18-crown-ether-6 and zirconium phosphate composite (ZrP/18C6) with a mass ratio of 1 : 1 was used for further study of $Sr^{2+}$ ions removal in the following studies.

**3.3.2 Effect of contact time.** Effect of the time of $Sr^{2+}$ adsorption by α-ZrP and ZrP/18C6 on the adsorption capacity was performed by sampling at various adsorption times of 5 min, 10 min, 20 min, 30 min, 60 min, 150 min, 240 min, 360 min, 1080 min, and 1440 min, respectively (Fig. 6(b)). With passing time, the adsorption rate increased and gradually reached equilibrium. In the beginning of the adsorption test, the rate of adsorption increased rapidly due to availability of a lot of adsorption sites in the material. When the adsorption continued, $Sr^{2+}$ concentration in the solution decreased and the free adsorption sites of the material gradually decreased, as a result, the adsorption rate decreased significantly. Fig. 6(b) shows that the adsorption of $Sr^{2+}$ on ZrP/18C6 reached equilibrium within 30 min, with a removal rate of 98.60%. Compared to ZrP/18C6, α-ZrP took about 360 min to reach the adsorption equilibrium with a removal rate of 13.80%. Therefore, the adsorption of ZrP/18C6 for $Sr^{2+}$ is quicker than that of α-ZrP and most zirconium phosphate-based inorganic adsorbents.[26,31,36] In the subsequent adsorption experiments, the contact time of 6 h was used to ensure that the adsorption reaches equilibrium.

**3.3.3 Effect of solution pH.** As nuclear liquid wastes can be formed under different pH conditions depending on where they are generated, in this test, the effect of pH on the adsorption of $Sr^{2+}$ on α-ZrP and ZrP/18C6 was performed by adjusting the pH of the solution from 2 to 10 using nitric acid and sodium hydroxide (Fig. 7(a)). When other conditions were same, the removal rate of α-ZrP improved correspondingly as the pH value increased from 2 to 10, with a maximum removal rate of 40% at pH 10. Although the removal rate of ZrP/18C6 was poor at pH 2, it rapidly increased to 98.62% at pH 3 and maintained a high value of greater than 97% in the pH range from 4 to 10. Therefore, the ZrP/18C6 composite demonstrates excellent adsorption performance in the removal of $Sr^{2+}$ in the pH range from 3 to 10. A large difference between α-ZrP and ZrP/18C6 in

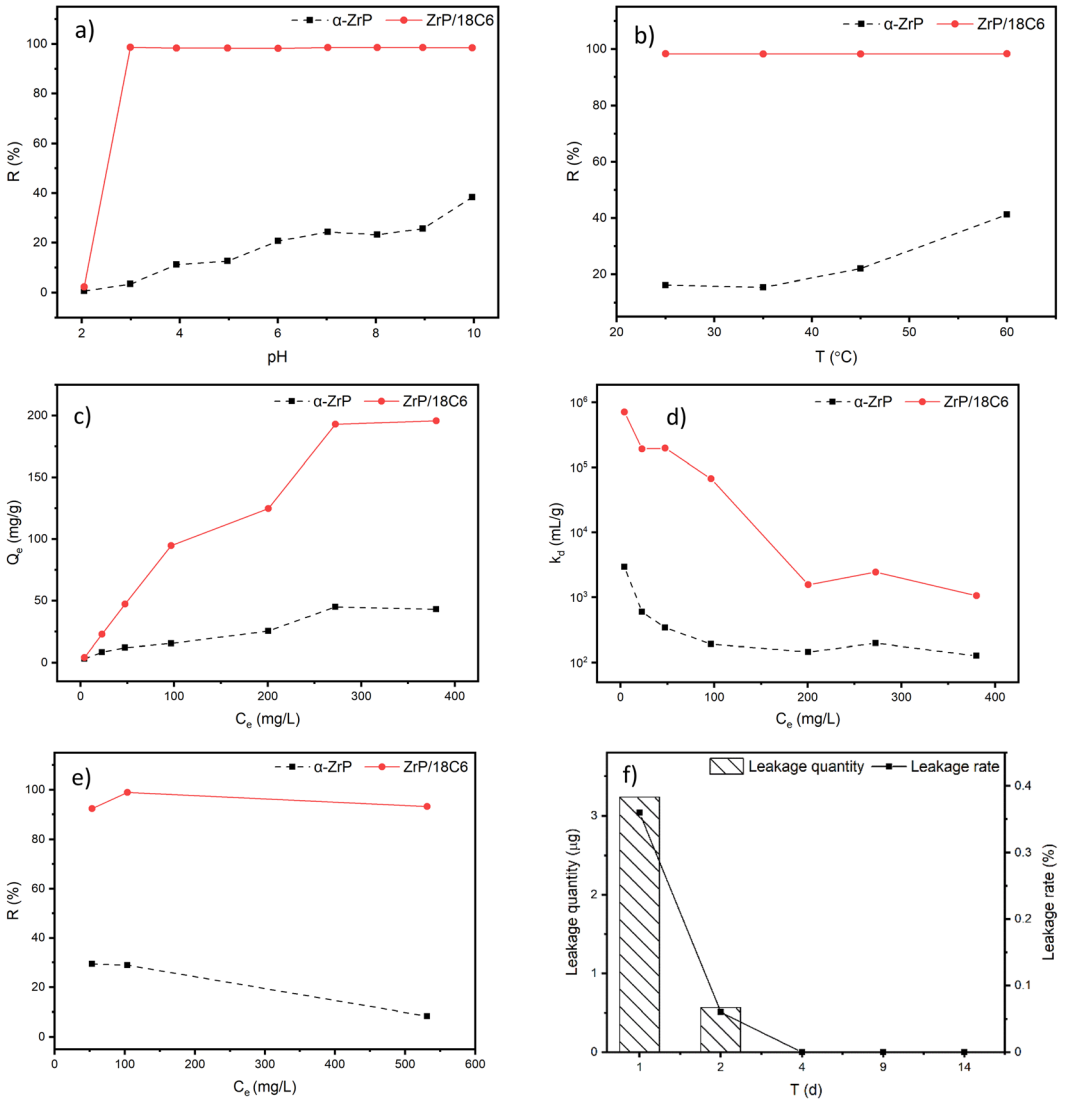


Fig. 7 (a) Effect of pH in the solution. (b) Effect of temperature in the solution. (c and d) Effect of $Sr^{2+}$ concentration. (e) Effect of competing ions concentration. (f) The leakage amount of $Sr^{2+}$ from ZrP/18C6 immersed water after $Sr^{2+}$ adsorption.

adsorption capacity is ascribed to the structure of ZrP/18C6 having the larger interlayer separation, which provides more adsorption sites for $Sr^{2+}$.[27] Subsequent adsorption experiments were carried out under the conditions at pH = 7.

**3.3.4 Effect of temperature.** The adsorption performance of an adsorbent is largely affected by the environmental temperature. To explore the effect of temperature on $Sr^{2+}$ adsorption by α-ZrP and ZrP/18C6, $Sr^{2+}$ adsorption was carried out at different temperatures (Fig. 7(b)). With the temperature rise, the adsorption rate of α-ZrP slightly increased while the adsorption rate of ZrP/18C6 almost maintained the same. This indicates that the temperature had no significant effect on the adsorption performance of ZrP/18C6 for $Sr^{2+}$.

**3.3.5 Effect of $Sr^{2+}$ concentration.** The different initial $Sr^{2+}$ concentration for adsorption was carried out to examine maximum adsorption capacity of α-ZrP and ZrP/18C6 at the equilibrium (Fig. 7(c) and (d)). The adsorption capacities of both α-ZrP and ZrP/18C6 for $Sr^{2+}$ gradually increased with increase in the equilibrium concentration of $Sr^{2+}$. When the equilibrium concentration of $Sr^{2+}$ was at 380 mg $L^{-1}$, the maximum adsorption equilibrium capacity of ZrP/18C6 for $Sr^{2+}$ was obtained to be 195.74 mg $g^{-1}$, which was 4.5 times higher than that of α-ZrP at 43.03 mg $g^{-1}$. It can be seen that ZrP/18C6 attains a higher adsorption capacity than the general zirconium phosphate-based materials[12] and crown ether-based materials,[14] indicating a better adsorption potential. This suggests that intercalation of 18-crown-ether-6 into zirconium phosphate leads to the formation of many binding sites for $Sr^{2+}$.[40] Meanwhile, when the equilibrium concentration of $Sr^{2+}$ was at low level less than 50 mg $L^{-1}$, value of the distribution coefficient ($K$) was higher than $1 \times 10^5$ mL $g^{-1}$, and when it was at 4.28 mg $L^{-1}$, the value of $K$ achieved $7 \times 10^5$ mL $g^{-1}$, which is greater than most $Sr^{2+}$ adsorbent materials.[12,26] This indicates that the ZrP/18C6 has a high affinity for $Sr^{2+}$ even though $Sr^{2+}$ is at low concentration level.

**3.3.6 Effect of competing ions.** The presence of competing ions in the solution might have an impact on the performance of an adsorbent in removing $Sr^{2+}$ due to interruption. As ionic radii of $Na^+$ and $K^+$ are close to that of $Sr^{2+}$, the effect of these two competing ions on the adsorption of $Sr^{2+}$ by α-ZrP and ZrP/18C6 was investigated. In the test, the $Sr^{2+}$ concentration was kept at 50 mg $L^{-1}$, and both $Na^+$ and the $K^+$ concentrations were adjusted to be 50, 100, and 500 mg $L^{-1}$, respectively (Fig. 7(e)). With increase in the competing ion concentration, the removal rate of $Sr^{2+}$ by α-ZrP significantly decreased while the removal rate of $Sr^{2+}$ by ZrP/18C6 only slightly decreased. Even though the concentrations of $Na^+$ and $K^+$ in the solution were 10 times higher than that of $Sr^{2+}$, the removal rate of $Sr^{2+}$ by ZrP/18C6 maintained more than 92% of the original value. Therefore, the adsorption performance of ZrP/18C6 for $Sr^{2+}$ is less affected by the competing ions, compared to α-ZrP. This is attributed to the special affinity of the 18-crown-ether-6 to $Sr^{2+}$.[19,34]

**3.3.7 Desorption studies.** How strongly the ions adsorbed on a material is important in evaluating its stability and applicability. After adsorption of $Sr^{2+}$ ions, the ZrP/18C6 composite was immersed in deionized water to take the samples on the 1st, 2nd, 4th, 9th, and 14th day, and the concentration of $Sr^{2+}$ in the solution was measured to examine the amount of $Sr^{2+}$ leaked without data cumulative (Fig. 7(f)). There was a small amount of $Sr^{2+}$ ions leaked from ZrP/18C6 on the 1st and 2nd days, after which no $Sr^{2+}$ leak was detected within the instrument detection limit. The total accumulated leakage amount was about 0.005 mg with a leakage rate of 0.5% in 14 days. This indicates the ZrP/18C6 adsorbent has a strong binding force for $Sr^{2+}$.

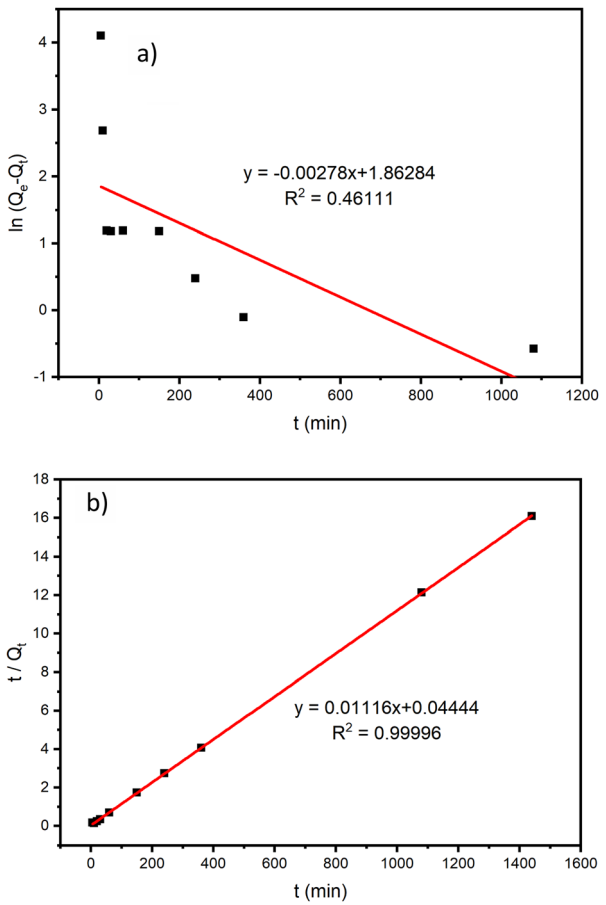


Fig. 8 Kinetic model fitting curves on $Sr^{2+}$ adsorption by ZrP/18C6. (a) Pseudo-first order kinetics model. (b) Pseudo-second order kinetics model.

### 3.4 Adsorption mechanism of $Sr^{2+}$ onto ZrP/18C6

**3.4.1 Adsorption kinetics study.** An adsorption kinetics is studied to examine by which adsorption process is dominated. In this study, two main kinetic models, the pseudo-first order model[44] and the pseudo-second order model,[45] are employed, as expressed with eqn (6) and (7), respectively.

$$\ln(Q_e - Q_t) = \ln Q_e - k_1 t \quad (6)$$

$$\frac{t}{Q_t} = \frac{1}{k_2 Q_e^2} + \frac{t}{Q_e} \quad (7)$$

where $Q_e$ (mg $g^{-1}$) and $Q_t$ (mg $g^{-1}$) are the adsorption capacity of ZrP/18C6 at adsorption equilibrium and at a certain adsorption time, respectively; $t$ (min) is the adsorption time; $k_1$ and $k_2$ are the adsorption rate constants of the pseudo-first order and the pseudo-second order kinetic models, respectively.

The adsorption data of the ZrP/18C6 adsorbent were fitted to the kinetic models (Fig. 8), and the corresponding model fitting parameters are obtained (Table 1). The adsorption data have a better fit to the pseudo-second order kinetic model with $R^2 =$ 0.99996 than the pseudo-first order model. Meanwhile, the equilibrium adsorption amount of 89.605 mg $g^{-1}$ obtained from the fitting is in good agreement with 89.51 mg $g^{-1}$ obtained from the experiment. It is concluded that the adsorption of $Sr^{2+}$ onto ZrP/18C6 proceeds with the pseudo-second order model.[46] Therefore, the adsorption process is dominated by chemisorption.[47]

**3.4.2 Adsorption thermodynamics study.** The adsorption thermodynamics of an adsorbent is studied to examine with which adsorption proceeds. The isotherm Langmuir adsorption model[48] and the Freundlich adsorption model[49] present monolayer and multilayer processes, respectively, as expressed with eqn (8) and (9) as follows.

Table 1 Kinetic model fitting parameters of $Sr^{2+}$ adsorption by ZrP/18C6

| Model | Pseudo-first order | | | Pseudo-second order | | |
|---|---|---|---|---|---|---|
| Modeling parameters | $Q_e$ (mg $g^{-1}$) | $k_1$ ($min^{-1}$) | $R^2$ | $Q_e$ (mg $g^{-1}$) | $k_2$ (g $min^{-1}$ $mg^{-1}$) | $R^2$ |
| Value | 6.442 | 0.0028 | 0.46111 | 89.605 | 0.0028 | 0.99996 |

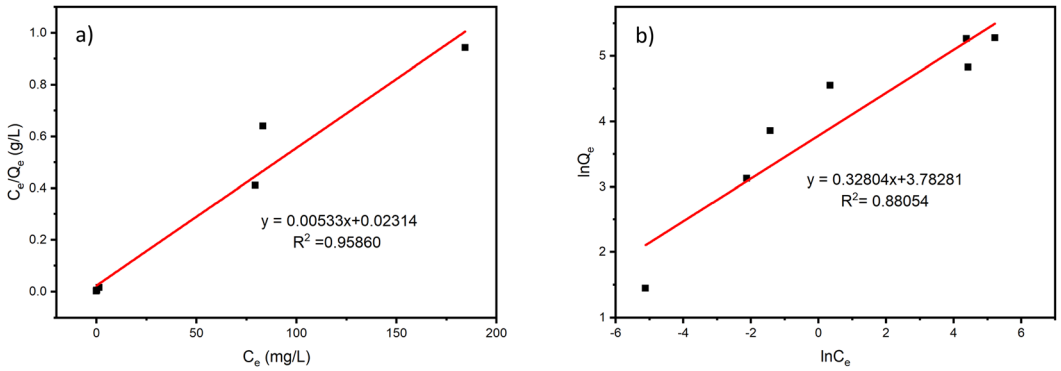


Fig. 9 Thermodynamics isotherm model fitting curves of $Sr^{2+}$ adsorption by ZrP/18C6. (a) Langmuir adsorption isotherm model. (b) Freundlich adsorption isotherm model.

$$\frac{C_e}{Q_e} = \frac{1}{k_L Q_m} + \frac{C_e}{Q_m} \quad (8)$$

$$\ln Q_e = \ln k_F + \frac{1}{n} \ln C_e \quad (9)$$

where $C_e$ (mg $L^{-1}$) is the concentration of $Sr^{2+}$ in solution at adsorption equilibrium; $Q_e$ (mg $g^{-1}$) is the adsorption capacity of the adsorbent at $Sr^{2+}$ adsorption equilibrium; $Q_m$ (mg $g^{-1}$) is the saturation adsorption capacity of the adsorbent for $Sr^{2+}$; $k_L$ (L $mg^{-1}$) and $k_F$ (L $mg^{-1}$) are the adsorption equilibrium constants of the isotherm Langmuir adsorption model and Freundlich adsorption model, respectively; $n$ is the heterogeneity factor, which is an empirical constant of adsorption related to the adsorption strength.

To further understand the adsorption process of $Sr^{2+}$ on ZrP/18C6, the adsorption data obtained at 25 °C were fitted to the models (Fig. 9), and the corresponding model fitting parameters were obtained (Table 2). It can be found that the isotherm Langmuir adsorption model is better fitted to the data with $R^2 =$ 0.95860 than the Freundlich adsorption model. Moreover, the equilibrium adsorption amount of 187.617 mg $g^{-1}$ obtained from the isotherm Langmuir adsorption model was closer to the experimental data of 195.74 mg $g^{-1}$. The theoretical model analysis indicates that the $Sr^{2+}$ ions are adsorbed onto the ZrP/18C6 composite mainly *via* the monolayer process.[50]

**3.4.3 Mechanism studies.** The XRD data show that α-ZrP is a layered structure with an interlayer separation of 0.76 nm, which is confirmed by the SEM morphology as presented in the Fig. 4. The presence of P–OH groups in the IR spectrum indicates that there are a lot of adsorption sites available for $Sr^{2+}$ ions. Intercalation of 18-crown-ether-6 into the room between the layers leads to expanding the interlayer separation to 1.871 nm, which can provide more adsorption sites for $Sr^{2+}$. Moreover, 18-crown-ether-6 is known as an adsorbent with a special affinity for $Sr^{2+}$.[34,37] Therefore, the ZrP/18C6 composite is expected to be a strong adsorbent for the removal of Sr isotopes from nuclear wastes.

The adsorption experiments conducted in this study confirm that the ZrP/18C6 composite has a high adsorption capacity at 195.74 mg $g^{-1}$ when the equilibrium concentration of $Sr^{2+}$ was at 380 mg $L^{-1}$, which is 4.5 times higher than α-ZrP. The XRD patterns of ZrP/18C6 before and after adsorption were compared (Fig. 10(a)). It is shown that after adsorption the diffraction peak at 4.72° was shifted to a higher angle of 4.93° peak. This indicates that the interlayer separation in the ZrP/18C6 structure became narrower after adsorption owing to the strong complexation of $Sr^{2+}$ with oxygen atoms in 18-crown-ether-6 and –OH groups in zirconium phosphate. As the smaller free interlayer space limit occurrence of multilayer adsorption, $Sr^{2+}$ ions are mainly adsorbed onto the ZrP/18C6 *via* the monolayer process, which is consistent with the isotherm Langmuir model.

The P 2p and O 1s XPS of ZrP/18C6 before and after $Sr^{2+}$ adsorption was collected (Fig. 10(b) and (c)). A shift of 0.62 eV in the P 2p peak and 0.47 eV in the fitted P–O bond of the O 1s peak were observed after $Sr^{2+}$ adsorption. These data confirm that strong binding of $Sr^{2+}$ to the P–O bond in zirconium phosphate is formed during the adsorption.[51,52] Meanwhile, a new peak at 529.32 eV appeared in the O 1s peak, which is ascribed to the Sr–O bond,[53] and the fitted C–O–C bond in the O 1s peak also changed by 0.47 eV after adsorption. These data suggest that 18-crown-ether-6 is involved in the adsorption process by reacting $Sr^{2+}$ with oxygen atoms in the crown ether.[40] Therefore, $Sr^{2+}$ are adsorbed onto ZrP/18C6 *via* the chemisorption process at a relatively high speed.

Table 2 Thermodynamics isotherm model parameters of $Sr^{2+}$ adsorption by ZrP/18C6

| Model | Langmuir | | | Freundlich | | |
|---|---|---|---|---|---|---|
| Modeling parameters | $Q_m$ (mg $g^{-1}$) | $k_L$ ($mg^{-1}$) | $R^2$ | $1/n$ | $k_F$ ($L^n$ $mg^{n-1}$ $g^{-1}$) | $R^2$ |
| Value | 187.617 | 0.230 | 0.95860 | 0.32804 | 43.939 | 0.88054 |

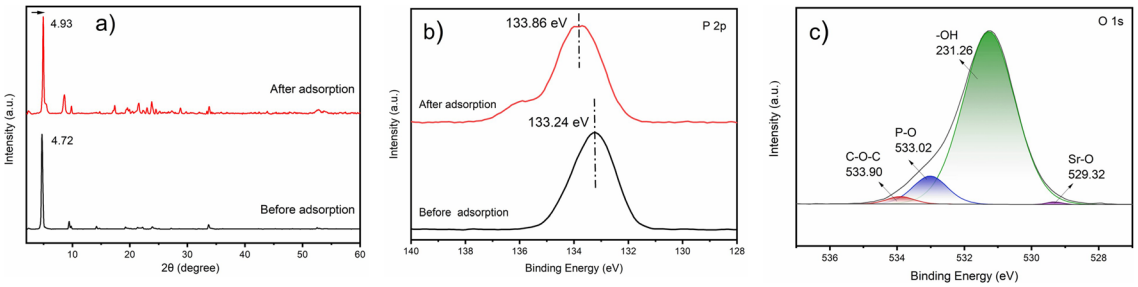


Fig. 10 The change of ZrP/18C6 before and after $Sr^{2+}$ adsorption (a) XRD patterns. (b) XPS spectra of P 2p. (c) XPS spectra of O 1s after $Sr^{2+}$ adsorption.

## 4 Conclusions

In the present study, zirconium phosphate/18-crown-ether-6 composite (ZrP/18C6) was successfully synthesized by expanding the interlayer space of α-ZrP with *n*-butylamine. The effects of the environmental factors and $Sr^{2+}$ concentration on the adsorption behavior of $Sr^{2+}$ onto ZrP/18C6 were systematically investigated to examine its adsorption performance and adsorption mechanism. The ZrP/18C6 composite demonstrates an excellent adsorption capacity of 195.74 mg $g^{-1}$ for $Sr^{2+}$ at the equilibrium concentration of 380 mg $L^{-1}$, which was little affected by the solution temperature, pH and competing ions. The material shows a quick adsorption rate of 98.6% within 30 min and a high affinity for $Sr^{2+}$ with a distribution coefficient of $7 \times 10^5$ mL $g^{-1}$ at a low $Sr^{2+}$ concentration of 4.28 mg $L^{-1}$. In addition, the composite adsorbent exhibits good thermal stability and acid resistance.

Analyses of the adsorption data, in combination with XRD and XPS data, reveal that $Sr^{2+}$ ions are adsorbed onto ZrP/18C6 *via* the Langmuir monolayer model that is mainly controlled by the chemisorption process. The desorption data show that $Sr^{2+}$ ions adsorbed onto the ZrP/18C6 material are well preserved with a low leakage rate of 0.5% in a 14 day experiment. Therefore, the layered zirconium phosphate/18-crown-ether-6 (ZrP/18C6) composite is a promising candidate adsorbent for application in the removal of $Sr^{2+}$ from nuclear waste streams. However, further experiments should be conducted on its stability under radiation conditions and its adsorption performance in actual nuclear waste streams.

## Author contributions

Lina Wu performed the experiments, analyzed the data and wrote the manuscript. Huiping Wang provided helpful discussions and performed the characterizations. Xiangqian Kong and Haibo Wei collected and analyzed the data. Sheng Chen reviewed the manuscript. Lisheng Chi revised the manuscript. All authors have given approval to the final version of the manuscript.

## Conflicts of interest

There are no conflicts to declare.

## Acknowledgements

This work was supported by Fujian Science & Technology Innovation Laboratory for Optoelectronic Information of China (#2021ZR108).

## Notes and references

1 R. Natarajan, *Prog. Nucl. Energy*, 2017, **101**, 118–132.
2 S. K. Sahoo, N. Kavasi, A. Sorimachi, H. Arae, S. Tokonami, J. W. Mietelski, E. Lokas and S. Yoshida, *Sci. Rep.*, 2016, **6**, 23925.
3 A. Burger and I. Lichtscheidl, *Sci. Total Environ.*, 2019, **653**, 1458–1512.
4 S. Pors Nielsen, *Bone*, 2004, **35**, 583–588.
5 Y. Guo, N. T. Hong Nhung, X. Dai, C. He, Y. Wang, Y. Wei and T. Fujita, *Front. Bioeng. Biotechnol.*, 2022, **10**, 819407.
6 P. N. Khan, A. Bhattacharyya, J. N. Sharma and S. Manohar, *J. Hazard. Mater.*, 2020, **397**, 122476.
7 M. A. Momen and M. L. Dietz, *React. Funct. Polym.*, 2021, **160**, 104829.
8 R. K. Vishwakarma, P. K. Narayanam, R. Umamaheswari and K. Sundararajan, *J. Environ. Manage.*, 2021, **298**, 113443.
9 Y. K. Kim, S. Kim, Y. Kim, K. Bae, D. Harbottle and J. W. Lee, *Appl. Surf. Sci.*, 2019, **493**, 165–176.
10 D. Sofronov, M. Rucki, V. Varchenko, E. Bryleva, P. Mateychenko and A. Lebedynskiy, *J. Environ. Chem. Eng.*, 2022, **10**, 106944.
11 S. Eun, J. Ryu, H. Kim, H. J. Hong and S. Kim, *J. Environ. Manage.*, 2021, **297**, 113389.
12 J. Zhang, L. Chen, X. Dai, L. Chen, F. Zhai, W. Yu, S. Guo, L. Yang, L. Chen, Y. Zhang, L. He, C. Chen, Z. Chai and S. Wang, *Chem. Commun.*, 2021, **57**, 8452–8455.
13 G. Kim, D. S. Lee, H. Eccles, S. M. Kim, H. U. Cho and J. M. Park, *RSC Adv.*, 2022, **12**, 18936–18944.
14 L. Yin, X. Kong, X. Shao and Y. Ji, *J. Environ. Chem. Eng.*, 2019, **7**, 103073.
15 S. İnan, *J. Radioanal. Nucl. Chem.*, 2022, **331**, 1137–1154.
16 D. Alby, C. Charnay, M. Heran, B. Prelot and J. Zajac, *J. Hazard. Mater.*, 2018, **344**, 511–530.
17 N. A. Bezhin, I. I. Dovhyi, S. V. Kapranov, N. I. Bobko, V. V. y. Milyutin, V. O. Kaptakov, E. A. Kozlitin and

I. G. Tananaev, *J. Radioanal. Nucl. Chem.*, 2021, **328**, 1199–1209.
18 B. Aguila, D. Banerjee, Z. Nie, Y. Shin, S. Ma and P. K. Thallapally, *Chem. Commun.*, 2016, **52**, 5940–5942.
19 E. P. Horwitz, M. L. Dietz and D. E. Fisher, *Solvent Extr. Ion Exch.*, 1990, **8**, 199–208.
20 M. Pica, A. Donnadio and M. Casciola, *Coord. Chem. Rev.*, 2018, **374**, 218–235.
21 A. Contreras-Ramirez, S. Tao, G. S. Day, V. I. Bakhmutov, S. J. L. Billinge and H. C. Zhou, *Inorg. Chem.*, 2019, **58**, 14260–14274.
22 A. Bashir, S. Ahad, L. A. Malik, A. Qureashi, T. Manzoor, G. N. Dar and A. H. Pandith, *Ind. Eng. Chem. Res.*, 2020, **59**, 22353–22397.
23 M. V. Ramos-Garcés, J. González-Villegas, A. López-Cubero and J. L. Colón, *Acc. Mater. Res.*, 2021, **2**, 793–803.
24 A. Clearfield and J. A. Stynes, *J. Inorg. Nucl. Chem.*, 1964, **26**, 117–129.
25 M. Pica, *Molecules*, 2021, **26**, 2392.
26 Z. Li, E. L. Vivas, Y. J. Suh and K. Cho, *J. Environ. Chem. Eng.*, 2022, **10**, 107333.
27 J. Zhang, L. Feng, Y. Jian, G. Luo, M. Wang, B. Hu, T. Liu, J. Li, Y. Yuan and N. Wang, *Chem. Eng. J.*, 2022, **429**, 132265.
28 W. Mu, Q. Yu, B. Chen, X. Li, H. Wei, Y. Yang and S. Peng, *J. Mol. Liq.*, 2021, **323**, 114585.
29 A. Clearfield and G. D. Smith, *J. Inorg. Nucl. Chem.*, 1968, **30**, 327–329.
30 A. Clearfield and R. M. Tindwa, *J. Inorg. Nucl. Chem.*, 1979, **41**, 871–878.
31 W. Mu, Y. Yang, B. Chen, X. Li, H. Wei, Y. Yang and s. Peng, *Sep. Purif. Technol.*, 2022, **291**, 120605.
32 H. X. Zhang, Z. X. Huang, P. Y. Zhao, Y. Hou, J. J. Guo and Y. C. Wu, *Mater. Res. Express*, 2019, **6**, 125095.
33 S. Avramescu, S. Petrescu, D. C. Culita, M. Tudose, A. Hanganu, I. Zarafu and P. Ionita, *J. Nanopart. Res.*, 2020, **22**, 194.
34 N. A. Bezhin and I. I. Dovhyi, *Russ. Chem. Rev.*, 2015, **84**, 1279–1293.
35 W. Mu, Q. Yu, J. Gu, X. Li, Y. Yang, H. Wei and S. Peng, *Sep. Purif. Technol.*, 2020, **240**, 116658.
36 W. Mu, B. Chen, Y. Yang, X. Li, H. Wei, Y. Yang and S. Peng, *J. Phys. Chem. Solids*, 2022, **163**, 110604.
37 J. D. Law, D. J. Wood and R. S. Herbst, *Sep. Sci. Technol.*, 1997, **32**, 223–240.
38 Z. Wei, Y. Gao, Y. Zhou, C. Jiao, M. Zhang, H. Hou and W. Liu, *J. Serb. Chem. Soc.*, 2020, **85**, 909–922.
39 W. Mu, B. Chen, Q. Yu, X. Li, H. Wei, Y. Yang and S. Peng, *J. Mol. Liq.*, 2021, **326**, 115307.
40 C. Guo, M. Yuan, L. He, L. Cheng, X. Wang, N. Shen, F. Ma, G. Huang and S. Wang, *CrystEngComm*, 2021, **23**, 3349–3355.
41 J. R. Ferraro, *J. Chem. Educ.*, 1961, **38**, 201.
42 S. Pourbeyram, *Ind. Eng. Chem. Res.*, 2016, **55**, 5608–5617.
43 S. M. Fernández-Valverde, A. Contreras-Ramírez, E. Ordóñez-Regil, M. E. Fernández-García and M. Pérez-Álvarez, *J. Solid State Chem.*, 2013, **198**, 238–245.
44 Y. S. Ho, *Scientometrics*, 2004, **59**, 171–177.
45 Y. S. Ho and G. McKay, *Process Biochem.*, 1999, **34**, 451–465.
46 Y. S. Ho, *J. Hazard. Mater.*, 2006, **136**, 681–689.
47 Y. S. Ho and G. McKay, *Process Saf. Environ. Prot.*, 1998, **76**, 332–340.
48 I. Langmuir, *J. Am. Chem. Soc.*, 1916, **38**, 2221–2295.
49 H. Freundlich, *Z. Phys. Chem., Stoechiom. Verwandtschaftsl.*, 1906, **57**, 385–470.
50 H. Swenson and N. P. Stadie, *Langmuir*, 2019, **35**, 5409–5426.
51 Z. Jiao, Y. Meng, C. He, X. Yin, X. Wang and Y. Wei, *Microporous Mesoporous Mater.*, 2021, **318**, 111016.
52 Q. Gao, J.-F. Xie, Y.-T. Shao, C. Chen, B. Han, K.-S. Xia and C.-G. Zhou, *Chem. Eng. J.*, 2017, **313**, 197–206.
53 J.-C. Dupin, D. Gonbeau, P. Vinatier and A. Levasseur, *Phys. Chem. Chem. Phys.*, 2000, **2**, 1319–1324.